

# A model of roof-top surface pressures produced by conical vortices : Evaluation and implications

D. Banks<sup>†</sup> and R. N. Meroney<sup>‡</sup>

*Fluid Mechanics and Wind Engineering Program, Civil Engineering Department,  
Colorado State University, Fort Collins, CO 80523, U.S.A.*

**Abstract.** The greatest suction on the cladding of flat roof low-rise buildings is known to occur beneath the conical vortices that form along the roof edges for cornering winds. In a companion paper, a model of the vortex flow mechanism has been developed which can be used to connect the surface pressure beneath the vortex to adjacent flow conditions. The flow model is experimentally validated in this paper using simultaneous velocity and surface pressure measurement on a 1 : 50 model of the Texas Tech University experimental building in a wind tunnel simulated atmospheric boundary layer. Flow visualization gives further insight into the nature of peak suction events. The flow model is shown to account for the increase in suction towards the roof corner as well as the presence of the highest suction at wind angles of 60°. It includes a parameter describing vortex suction strength, which is shown to be related to the nature of the reattachment, and also suggests how different components of upstream turbulence could influence the surface pressure.

**Key words:**

---

## 1. Introduction

Severe peak negative pressures beneath the reattaching shear layer along the edge of a building's roof are attributable to vortices which form stably for cornering winds (Ginger and Letchford 1992) and sporadically for winds normal to the roof edge (Saathoff and Melbourne 1989). The need for a better understanding of the vortex flow mechanism was noted in both cases (Marwood and Wood 1997, Melbourne 1993). To that end, a model of the dependence of the surface pressure beneath the vortex on local flow parameters such as wind speed and direction was developed at Colorado State University (CSU).

This paper uses experimental measurements to evaluate this vortex flow mechanism model, which is fully developed in a companion paper (Banks and Meroney 2000b). This flow model is embodied in the Eqs. (1a) and (1b), where many of the terms are either illustrated in Fig. 1, or are discussed in the model development summary which follows. A table of nomenclature is also included in this paper, as several new symbols are introduced.

$$C_{p_s}(t) = \left( \frac{U_{spin}(t)}{\bar{U}_{spin}} \right)^2 \left( 1 - \frac{\bar{U}_M^2}{\bar{U}_{ref}^2} [1 + \sin^2(\alpha(t)) \cdot g(t)] \right) \quad (1a)$$

---

<sup>†</sup>

<sup>‡</sup> Professor

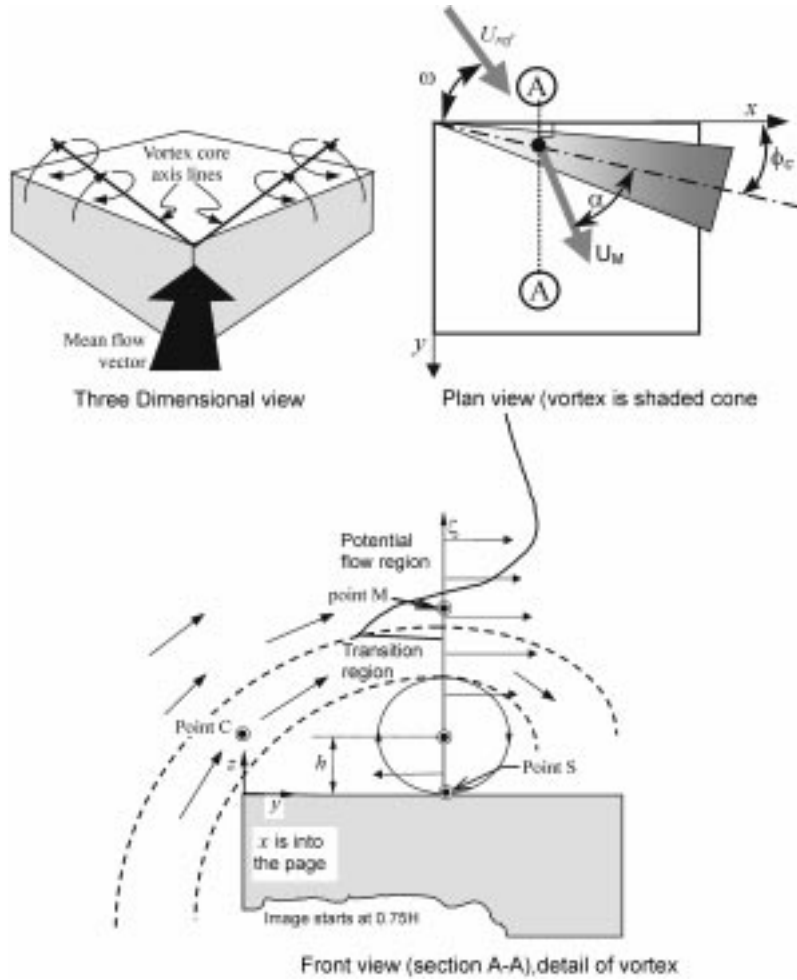


Fig. 1 Illustration of the terms used in the flow model equations. Also shown is the expected velocity profile through the vortex core.  $\zeta = 0$  at the vortex core

$$C\bar{p}_s = \left( 1 - \frac{\bar{U}_M^2}{\bar{U}_{ref}^2} [1 + \sin^2(\bar{\alpha}) \cdot g(\bar{\omega})] \right) \quad (1b)$$

The quantity  $U_{spin}$  is the speed at which the vortex rotates, and is considered to be linked directly to the flow speed directly outside of the separated flow zone, such as at the points  $M$  or  $C$ . The term  $U_{[subscript]}$  in general refers to a flow speed at a location described by the subscript, such as the point  $M$  or the reference location (upstream at roof height). This subscript convention is also used to describe the location at which a  $Cp_{[subscript]}$  value is being measured, so that  $Cp_s$  is the pressure coefficients measured at the points  $S$ . It is important to note that since the vortex moves in time, and the points  $M$  and  $S$  are directly beneath and above the vortex core respectively,  $Cp_s$  and  $U_M$  cannot be measured with a single stationary tap or velocity probe. This is discussed in more detail in section 2.2.

The development of the model embodied by Eq. (1) is based on the following reasoning :

- $C_{p_M}$  is assumed to be determined uniquely by the flow velocity at the point  $M$ , in keeping with the application of the steady Bernoulli equation to a region of potential flow :

$$C\bar{p}_M = 1 - \frac{\bar{U}_M^2}{\bar{U}_{ref}^2}$$

- The pressure minimum at the vortex core can be calculated from the radius of curvature and the tangential velocity through the vortex using the equation

$$\frac{dP}{dn} = \frac{\rho U^2}{R_c}$$

where  $n$  in a unit normal to the curving flow streamlines,  $R_c$  is the radius of curvature of the flow in and above the vortex,  $P$  is the static pressure and  $\rho$  is the air density.

- The mechanism by which the high suction at the core is partially transferred to the roof surface is as follows: The radius of curvature increases much more rapidly beneath the core than above it, because the roof forces the streamlines beneath the vortex to flatten out quickly. As a result, some of the very low pressure at the core is passed on to the surface. This mechanism is quantified in the calculation of  $g$ , which is reviewed briefly later in this paper.
- The faster the component of wind normal to the vortex core ( $U_M \cdot \sin(\alpha)$ ), the faster the vortex spins, so the greater the pressure drop to the core and to the surface for a given value of  $g$  :

$$C\bar{p}_M - C\bar{p}_S = \frac{\bar{U}_M^2}{\bar{U}_{ref}^2} \cdot \sin^2(\bar{\alpha}) \cdot g(\bar{\omega})$$

Since the flow speed at  $M$  controls both  $C_{p_M}$  and the lower value of  $C_{p_S}$  simultaneously, the vortex can be seen as an amplifier of the velocity related pressure drop at  $M$ . For this reason, the term ' $g$ ' is referred to as the amplification factor.

The experiments used to assess how well this model explains known vortex behaviour are described below.

## 2. Experimental procedures

### 2.1. Configuration of apparatus

Simultaneous measurement of surface pressures and flow velocities was performed in the CSU Meteorological Wind Tunnel. In some instances, flow images were recorded concurrently.

For this flow visualization, a laser light sheet was used to illuminate a plane within the flow separation region. The laser is a Coherent Innova 70-5 argon ion water-cooled laser, with a nominal maximum output of 5 Watts. The power level was set between 1 Watt and 2 Watts for these tests. Flow motions were exposed with glycerine smoke, which was introduced either upstream or through holes near the windward corner, or 'apex', of a model's roof. The digital recording system made use of a Pulnix TM-7CN CCD array camera, which provides one grey scale image every 1/60th of a second. The camera has a variable shutter speed, providing exposure times ranging from 1/60th of a second to 1/10,000th of a second. The shutter speed was generally set at either 1/125th or 1/250th of a second, so that the image effectively provides an average of the vortex position over this period of time. The camera's 60 Hz video signal was digitized by means of an Imaging Technology Inc.(ITI)

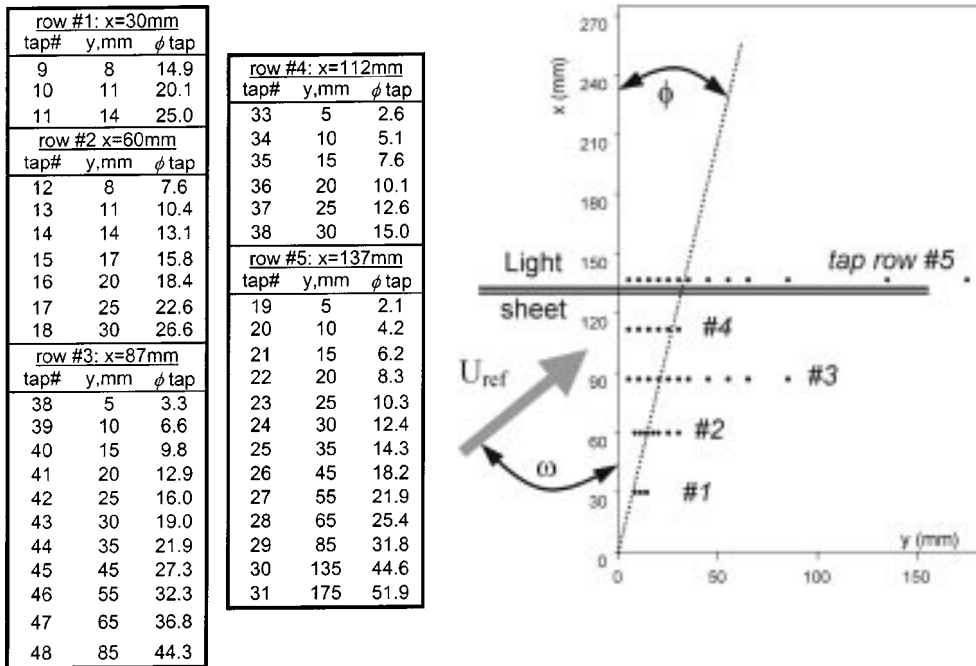


Fig. 2 Top view of 1:50 model of TTU WERFL building showing position and numbering to roof-top pressure taps used in this experiment

MVC IC Image video capture board installed in a PC. Real-time image acquisition and processing, as well as batch image post-processing, were performed using ITI's Itex-IC c-language libraries.

A 1:50 scale model of the TTU field site low-rise building was used for tests in the simulated ABL developed by Ham and Bienkiewicz (1998). The pressure tap layout for the 1:50 model is given in Fig. 2. In order to provide a suitably large vortex during the visualization, the light sheet was positioned at  $x = 137$  mm. This corresponds to  $x/H = 1.72$ , where  $x$  is the distance along the leading edge from the apex, and  $H$  is the building model's height.

The 0.5 mm diameter taps were connected to a 48-channel Pressure Systems Inc. (PSI) ESP48 pressure sensor transducer unit mounted inside the model. The restrictor tubes used with the PSI transducers provided a linear phase shift and a gain of  $1.0 \pm 0.1$  out to 200 Hz. A restrictor cut-off at 200 Hz was chosen to avoid cutting off any pressure peaks (Ham 1998). The pressures were recorded at a frequency of 480 Hz per tap. (Transducer settling time issues prevented pressure data collection as rates much above 500 Hz). Since all 48 signals exit the transducer on the same line, there was no possibility of low-pass filtering the signals electronically.

Velocities were measured using model 1210 single wire and model 1241  $\times$ -wire hot-film probes from Thermal Systems Inc. (TSI) connected to TSI model 1050 constant temperature anemometers. A typical arrangement was to place an  $\times$ -wire upstream and another  $\times$ -wire either above the leading edge (the point C) or directly above a selected pressure tap. All probes were aligned with the local mean flow vector. Tests were performed to ensure that the glycerine smoke used for visualization did not affect the mean or rms velocity measurements.

Time series of 50 seconds in duration ( $\approx 42$  minutes at full scale) were typically recorded for the pressure/velocity data. When images were also recorded, the data sequences were limited to 6

seconds in duration due to the considerable memory requirements of real-time image storage.

The wind tunnel free stream velocity was typically set at 8 m/s at building height. This provided an adequate pressure signal, while still leaving enough smoke in the visualization plane for flow structures to be discerned in the digital images.

A single TTL switch triggered data acquisition. A precisely timed LED sequencer placed inside the Plexiglas model was used to ensure synchronization between images and pressures. The restrictor tubing and the analog filters also introduce delays which were measured and corrected for during post processing.

## 2.2. Conditional sampling

One of the main conclusions from examining the vortex image sequences is that the vortex changes position and size rapidly and considerably in turbulent flow. A good deal of this motion is attributable to changes in the local wind direction, because the vortex core angle,  $\phi_c$ , is a function of the wind angle,  $\omega$  (Banks *et al.* 2000). ( $\phi_c$  and  $\omega$  are illustrated in Fig. 1;  $\omega$  is defined as the wind angle with respect to the roof edge along which the vortex of interest has formed, with  $\omega = 90^\circ$  for flow normal to this edge.  $\phi_c$  is the vortex core angle with respect to this same roof edge.) However, there is also random scatter in  $\phi_c$  about the mean for any given instantaneous wind direction (Banks and Meroney 2000a). Eq. (1b) predicts the surface pressure at a point beneath the moving vortex core, based on the flow velocity directly above the moving vortex core. To validate this equation, simultaneous flow velocity and surface pressure measurements are required along the  $\zeta$ -axis (which is a vertical line through the core of the vortex joining the points  $M$  and  $S$ , with  $\zeta = 0$  at the vortex core). Since  $\phi_c$  moves somewhat randomly, so does the  $\zeta$ -axis, which makes it impossible to take measurements at the points  $M$  and  $S$  with a single stationary probe or tap.

This problem was overcome by using conditional sampling. By simultaneously measuring the pressures at every tap in a given row, the location of the vortex could be ascertained, since the core is always above the location of maximum suction. The  $\times$ -wire probe was positioned above a target tap, one with a high likelihood of having the peak suction. By selecting only those pressure and velocity measurements in the time series when the target tap had the lowest pressure in the row, a discontinuous time series of  $U_M$  and  $Cp_S$  was extracted from the full time series. Such conditionally sampled time series were used to generate all of the plots in this paper.

## 2.3. Selection of the point $M$

The correlation between the flow speed along the  $\zeta$ -axis above a target tap and the pressures measured by that target tap reaches a maximum just above 3 times the mean core height,  $\zeta = 3\bar{h}$  (Fig. 3). Since the correlation drops off quickly for  $z < 3\bar{h}$ , the  $U_M(t)$  velocity measurements used to assess the validity of Eq. (1a) were taken at  $z \approx 3.5\bar{h}$ , where the correlation coefficient is typically at its maximum of  $\sim 0.8$ .

Another reason to place the probe at  $z > 3\bar{h}$  is that the probe was observed to alter the location of the vortex core when placed at  $z < 2.5\bar{h}$ , moving the mean vortex position closer to the roof edge. This shift in mean vortex position due to probe interference does not explain the loss of correlation for  $z_M < 3\bar{h}$ , however, because the conditional sampling process ensures that the vortex core is above the target tap and below the hot film for the data used in Fig. 3. One possible explanation is that the loss of correlation between  $U_M$  and  $Cp_S$  is due to changes in the vortex core height. It is known that

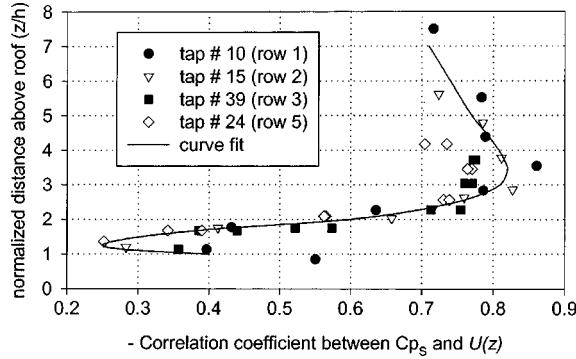


Fig. 3 Correlation between surface pressure and flow velocity above various target taps for a wind angle of  $55^\circ$

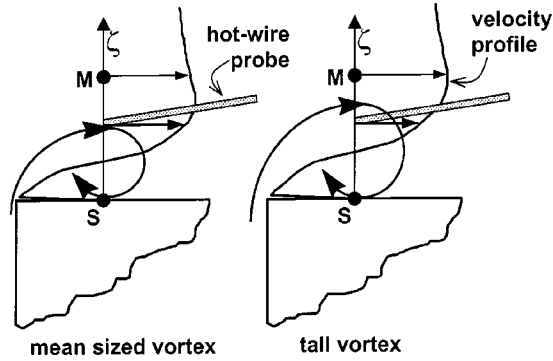


Fig. 4 Effect of hot wire position on total velocity

the vortex height for a given  $\phi_c$  can vary as much as 50% from the mean (Banks *et al.* 2000). If the velocity is being measured, for example, at twice the mean core height, then a larger than average value of  $h(t)$  will produce a considerable drop in the measured velocity (see Fig. 4). Without some knowledge of  $h(t)$ , this drop in velocity is indistinguishable from a decrease in local velocity. (The point ‘M’, also shown in Fig. 4, will likewise suffer some inaccuracy in  $U_M$  as a result of changes in  $h(t)$ , but it is expected to be less severe than for  $z < 3\bar{h}$ .) This uncertainty about  $h(t)$  imposes on the velocity signal random fluctuations that are unrelated to the overall flow speed at the roof edge, resulting in a loss of correlation.

### 3. Results

#### 3.1. Velocity and curvature profiles

The companion paper defines  $g$  as  $g(t) = g_s \cdot I_\delta(t)$ , where  $I_\delta$  is a delta function which is 0 when the vortex is absent, and  $g_s$  can be calculated by the equation

$$g_s = 2 \int_S^M \left( \frac{U(a)}{U_M} \right)^2 \cdot \left( \frac{R_c(a)}{h} \right)^{-1} da \quad (2)$$

where  $a = \zeta/h = (z-h)/h$  and  $R_c$  is the radius of curvature. In the companion paper, the functions  $U(a)/U_M$  and  $R_c(a)/h$  were estimated from the results of numerical delta wing vortex studies and heuristic arguments, and a value for  $g_s$  of  $\sim 1.5$  was determined. (Note that the location of the point  $M$  in the experimental work (at  $z = 3.5\bar{h}$ ) is slightly above the position of the point  $M$  used in the companion paper to derive the theoretical value of  $g(z = 3.1\bar{h})$ . This increases the expected value of  $g$ , from just below 1.5 to just above 1.5.)

The mean velocity profile could not be reliably measured for  $z < 1.5\bar{h}$  using the above facilities, since the hot-film probes cannot detect a flow reversal. The conditionally sampled mean velocity profiles do show reasonable agreement with the general shape of the estimated function for  $z > 1.5\bar{h}$ , however, as shown in Fig. 5. The sensitivity of Eq. (2) to variations in the velocity profile near the core was assessed, and showed that while the pressure at the vortex core depends greatly on the velocity profile, the surface pressure is less affected because of the expected relative symmetry of  $U(a)$  above and below the core.

In the potential flow zone, values of  $R_c(a)$  can be calculated from the velocity profiles since the flow is assumed to obey Bernoulli's equation. Since the pressure drop across the curved streamlines is prescribed by

$$\frac{dP}{da} = \frac{\rho U^2}{R_c}, \text{ the radius of curvature can be estimated as } R_c \approx \frac{-2 \cdot \Delta z \cdot U^2}{\Delta(U^2)}.$$

These calculations indicate that  $R_c$  can only be normalized by  $h$  close to the vortex core (perhaps only for  $z < 3\bar{h}$ ), because outside of this region the local curvature is determined by the overall flow over the building regardless of the vortex size (see Fig. 6). Fig. 6 also indicates that  $R_c$  above the core increases roughly with  $z^3$ .

In and around the transition region, the radius of curvature has been estimated from flow visualization images. A sample image is provided in Fig. 7, where the simultaneously measured pressure profiles have been superimposed during post-processing. The building model is the black rectangle in the lower left, upon which the location of the pressure taps in row #5, illustrated by 11 vertical white lines, has also been superimposed. The roof of the model represents  $C_p = 0$ , and the bottom of the image corresponds to  $C_p = -2.4$ , as indicated. The order in which each of the coloured  $C_p$  profiles

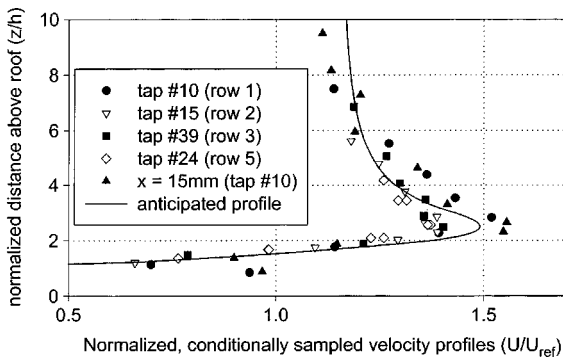


Fig. 5 Normalized velocity profiles above various target taps for  $\omega = 55^\circ$

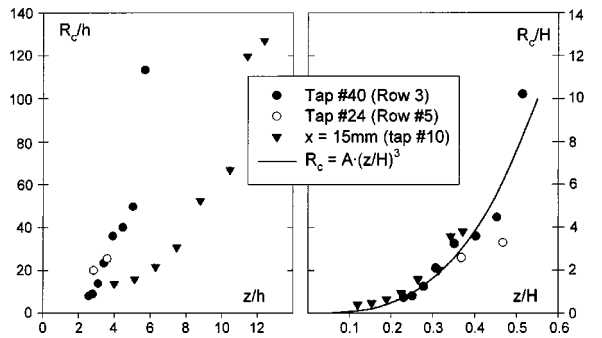


Fig. 6 Radius of curvature ( $R_c$ ) for several target taps, as a function of height above the roof  $R_c$  was calculated from velocity profiles.  $h$  = vortex core height,  $H$  = building height

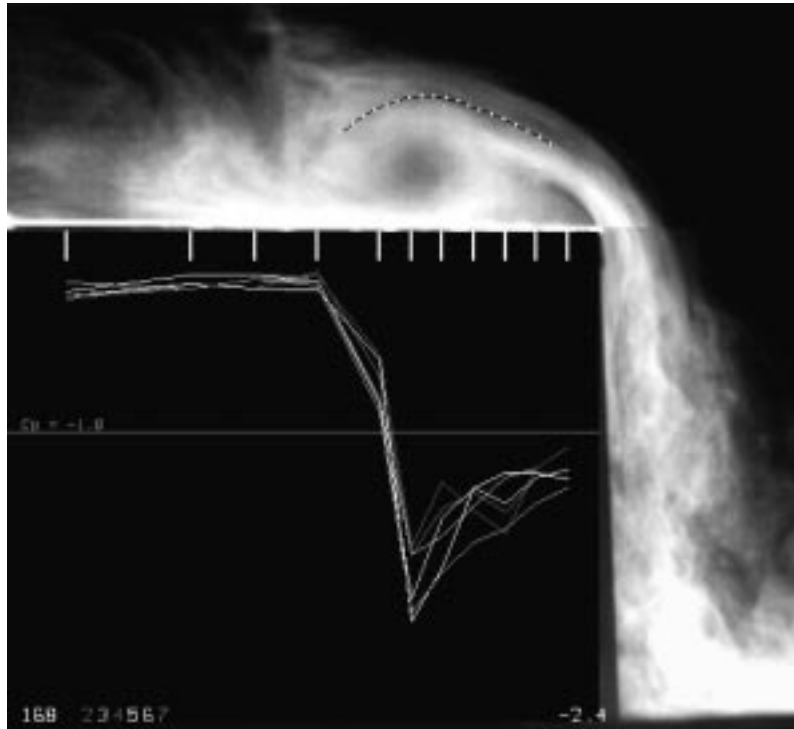


Fig. 7 Vortex image in smooth flow for  $\omega = 45^\circ$ , with tap locations and pressure profile superimposed. The dotted yellow line was used to calculate curvature.

occurred is given by the correspondingly coloured numbering in the lower left of the image. (Also in the lower left is image number, in this case 168; the sequence includes a total of 240 images taken over 4 seconds, for a sample rate of 60 Hz. The exposure time for this image was 8 ms.)

By selecting points that follow the flow, such as those indicated by the dotted line in Fig. 7, and fitting a curve to those points, the curvature could be calculated and normalized by the vortex core height. Data points derived by this technique are shown in Fig. 8. The points were fit by a curve of the form  $R_c/h = a + B \cdot a^3$  in Eq. (2) so that  $R_c$  approaches  $z$  in the limit as  $a \rightarrow 0$  and varies with  $z^3$  as  $a$  becomes large.

By varying the value of  $B$ , the sensitivity of  $g_s$  in Eq. (2) to variations in  $R_c(a)/h$  was assessed, using the velocity profile depicted in Figs. 1, 4 and 5. Some results are presented in Fig. 9, showing that higher relative curvature (lower  $R_c/h$ ) should produce greater values of  $g_s$ , and hence greater rooftop suction. The influence of curvature above the vortex will again be discussed once values of  $g$ , which have been indirectly measured using Eq. (1), have been presented.

### 3.2. $C_p$ as a function of distance from the corner

A comparison of the data series for the different rows of taps in Fig. 5 also indicates that  $U_M$  increases with decreasing  $x$ . This trend is supported by LDA measurements above a 200 mm cube, where it was reported that velocities in the conical vortex increase as the apex is approached (Minson and Wood 1992). The  $U_M$  vs.  $x$  relationship was quantified by further measurements taken

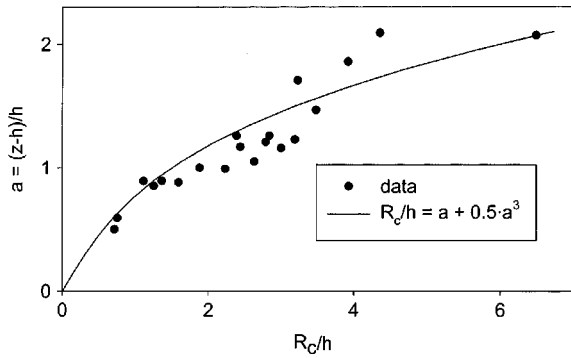


Fig. 8 Radius of curvature in the transition region, as determined from flow visualization for smooth flow and turbulent flow when  $1.0 < g_s < 1.5$

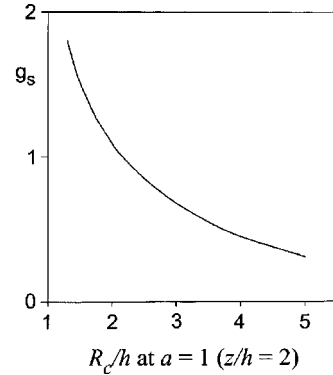


Fig. 9 Change in vortex amplification factor with curvature above the core, as indicated by  $R_c/h$  at  $a = 1$ . Calculations are based on  $R_c/h = a + B \cdot a^3$

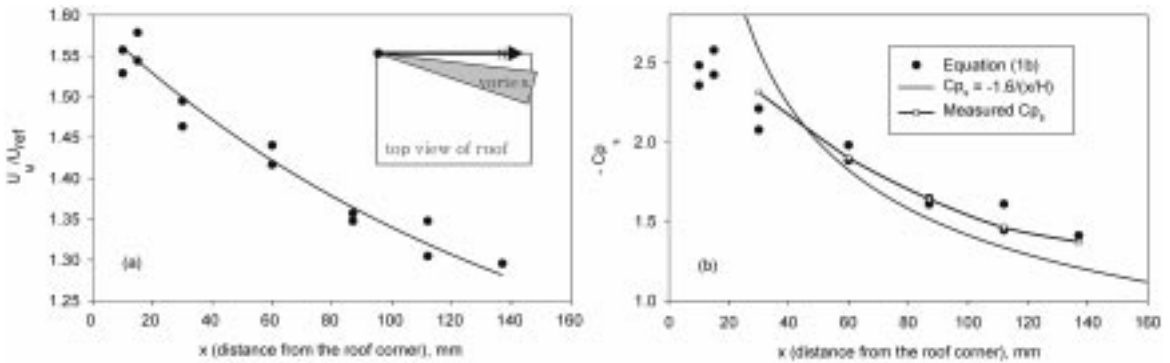


Fig. 10 Increase in velocity and surface pressure coefficient towards the roof corner.  $U_M$  was measured at  $z = 3h$  in this case.  $\omega = 55^\circ$

between  $z = 2h$  and  $z = 3h$  at several  $x$  positions for  $\omega = 55^\circ$ . Measurements were also taken at  $x = 15$  mm and  $x = 10$  mm, using tap #10 as the target tap to determine vortex position. The results are shown in Fig. 10a. For  $x < 15$  mm, the vortex becomes quite small ( $h < 2.5$  mm); hence, the peak velocity is probably slightly higher than what is measured, since when the measurement volume of the  $\times$ -wire is comparable to  $h^3$ , the wire will average velocities over a range of  $\pm h/2$ .

Substituting these  $U_M(x)$  values into Eq. (1b) produces Fig. 10(b), where  $g = 0.65$  has been used. (It is shown later in this paper that this is the expected mean value of  $g$  for  $\omega = 55^\circ$ ) This compares favourably with the measured increase in  $|C_{p_s}|$  towards the corner. ( $C_{p_s}$  is determined for a given  $x$  by extracting the minimum  $C_p$  from the row of taps at  $x$  for each point in time, and averaging this new time series.) The pressure coefficient beneath the vortex core is expected to decrease according to an equation of the form  $C_{p_s} = -C_1(x/H)^{-0.5}$  (Lin *et al.* 1995), and such a curve is also shown for comparison.

Why would the velocity increase towards the apex? One possibility is that while the normalized curvature at  $M$  might remain constant, the absolute value of the curvature must decrease as  $x \rightarrow 0$ , and the vortex gets linearly smaller. Since the flow speed increases inversely with  $R_c$  in a potential

flow region,  $U_M/U_{ref}$  would be expected to increase near the leading corner, or apex. So the smaller vortices would induce a greater absolute curvature at  $M$ , leading to a lower  $Cp_M$ . This analysis is also corroborated by the authors' observation of increased suction beneath smaller vortices in smooth flow (Banks *et al.* 2000), even though these vortices had identical  $R_c/h$  values at  $z = 2.2h$ .

### 3.3. $Cp$ as a function of wind direction

#### 3.3.1. Velocity components as a function of wind direction

Velocity profiles above a target tap were also measured for a range of wind directions, and the results are shown in Fig. 11a. The velocity above the vortex increases dramatically as the nominal wind angle is increased from  $15^\circ$  to  $60^\circ$ , at which point it levels off and begins to decrease (Fig. 11b). This helps to explain the general pattern of  $Cp_S$  vs. wind direction, which has a widely accepted worst case wind angle range of  $55^\circ < \omega < 60^\circ$ . Fig. 12 illustrates the maximum in  $Cp_S$  occurring at  $\omega = 60^\circ$  for row # 3 ( $x/H = 1.1$ ). Recall that the  $Cp_S(t)$  time series for row #3 represents the worst suction measured for all taps in row #3 at each point in time. Also shown for comparison is the value of  $|Cp(\omega)|$  for tap #39, which is located at  $\phi = 7^\circ$ . (This 'single tap  $Cp$  vs.  $\omega$ ' plot is a type more commonly found in literature). As one might expect, the value of  $|Cp|$  for the single tap is lower than  $|Cp_S|$  at all wind angles.

One interesting fact about the plot of  $|Cp(\omega)|$  for tap #39 is that even though the mean vortex position is above this tap at  $\omega = 35^\circ$ , (Banks *et al.* 2000) (and peak suction is always beneath the vortex core), the suction continues to increase with  $\omega$ , reaching its peak suction at  $\omega = 60^\circ$ . This can be explained using Eq. (1). Even though Eq. (1) is meant to predict  $Cp_S$  for a tap row perpendicular to the leading edge, it can be adapted for use on a single tap by using a transfer function (Banks and Meroney 2000a). The results show that the continued increase in  $|Cp|$  at tap #39 after the mean vortex core position has passed across the tap is due to the  $\alpha(\omega)$  and  $U_M(\omega)$  terms, which both continue to increase from  $\omega = 35^\circ$  to  $\omega = 60^\circ$ .

Even with the value of  $U_M$  reaching a maximum at  $\omega = 60^\circ$ , however, Eq. (1b) predicts that if  $g$  is a constant, then the suction should continue to increase as  $\omega \rightarrow 90^\circ$ . The  $Cp_S(\omega)$  curve calculated using Eq. (1b), with  $\alpha(\omega)$  given by  $\alpha = 18^\circ + 0.7\omega$  (Banks and Meroney 2000b),  $U_M$  as in Fig. 11b,

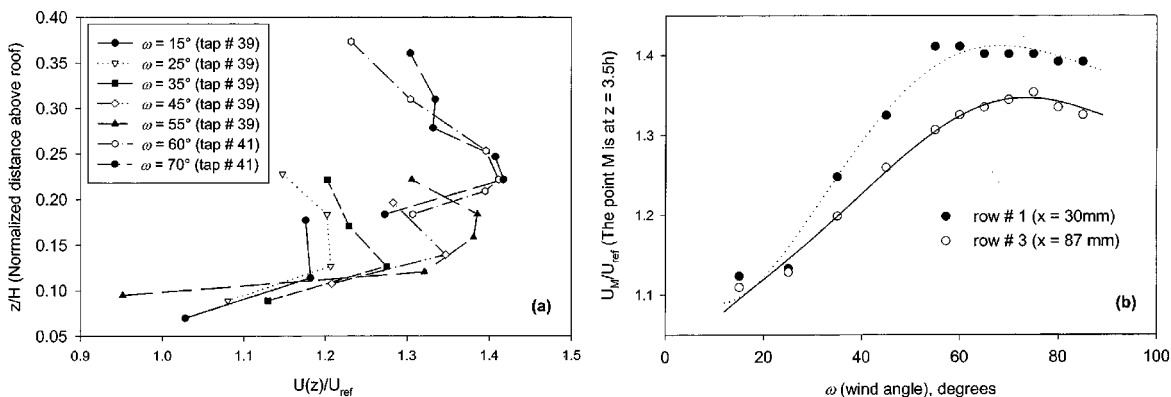
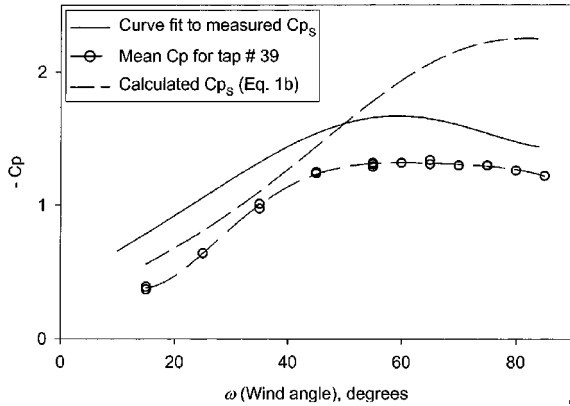
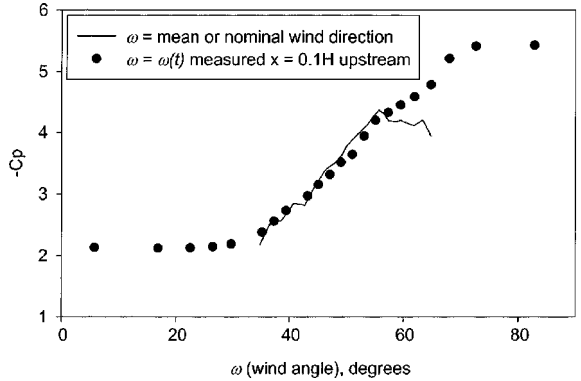


Fig. 11 Effect of wind angle upon the velocity above the vortex


 Fig. 12 Mean  $C_p$  beneath the vortex for tap row #3

 Fig. 13 (Letchford and Marwood 1997):  $C_p$  vs. wind angle for a tap at  $x = 0.05H$  and  $\phi = 16^\circ$ . The  $\omega(t)$  measurements were taken with a nominal wind direction of  $45^\circ$ 

and  $g = 0.65$  is also shown in Fig. 12.

However, if  $\omega(t)$  is measured  $0.1H$  upstream of the leading edge, and  $C_p$  is plotted against  $\omega(t)$  instead of mean wind direction, then the maximum suction does occur at  $80^\circ < \omega < 90^\circ$ , as shown in Fig. 13 (Letchford and Marwood 1997). This suggests that  $C_{p_s}$  does indeed vary with  $\sin^2(\alpha(t))$  for  $\omega(t) > 60^\circ$ . The fact that  $C_p$  does not drop off for instantaneous changes in wind direction from  $45^\circ$  to  $75^\circ$ , but does for a similar shift in mean wind direction, is in part attributable to an error in the quasi-steady(Q-S) assumption underlying Eq. (1a). Q-S theory assumes that an instantaneous change in wind direction has the same effect on the vortex as a long-term change in wind direction between the same angles. This is not the case for  $\omega(t) > 60^\circ$ , since the vortex is much more stable at low mean wind directions, and this translates into higher values of  $C_{p_s}$  for  $\omega(t) > 60^\circ$  when  $\bar{\omega} < 60^\circ$  (Banks 2000). This suggests that peak suction events are related to stable vortices at momentarily high local wind angles. The issue of the duration of a wind direction shift is explored further in the final section of this paper.

### 3.3.2. Amplification factor ( $g$ ) as a function of wind direction

The mean value of  $g$  is expected to decrease as  $\bar{\omega}$  approaches  $90^\circ$ , because flow visualization has shown that the vortex becomes increasingly unstable and intermittent. This accounts for the discrepancy between the measured  $C_{p_s}$  and that calculated using a constant  $g$  in Fig. 12. A function  $g(\omega)$  can be calculated from the measured and calculated  $C_{p_s}$  curves in Fig. 12, and it is shown in Fig. 14. If a value of  $g = 1.5$  is associated with a stable vortex, then an intermittency function  $I(\omega)$  can be calculated from  $g(\omega) = 1.5 \cdot I(\omega)$ ; this function is also displayed in Fig. 14.

Up to this point, we have focused upon the mean value equation, Eq. (1b). However, since the  $\times$ -wire at  $M$  can be used to measure  $\alpha(t)$  and  $U_M(t)$  and  $U_M(t)$  can be used for  $U_{spin}(t)$ , we can calculate the value of  $g(t)$  for each point in the time series using Eq. (1a). Since the point  $M$  is being used to measure the ‘spin’ velocity, and  $U_M$  is a function of  $\omega$ , Eq. (1a) becomes

$$C_{p_s}(t) = \left( \frac{U_M(t)}{\bar{U}_M(\omega(t))} \right)^2 \left( 1 - \frac{\bar{U}_M^2(\omega(t))}{\bar{U}_{ref}^2} [1 + \sin^2(\alpha(t)) \cdot g(t)] \right) \quad (3)$$

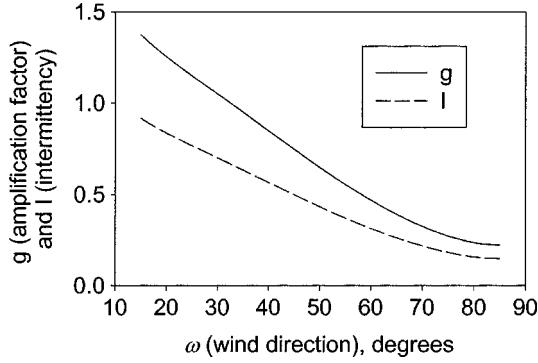


Fig. 14 Mean  $g(\omega)$  and  $I(\omega)$  for tap row #3

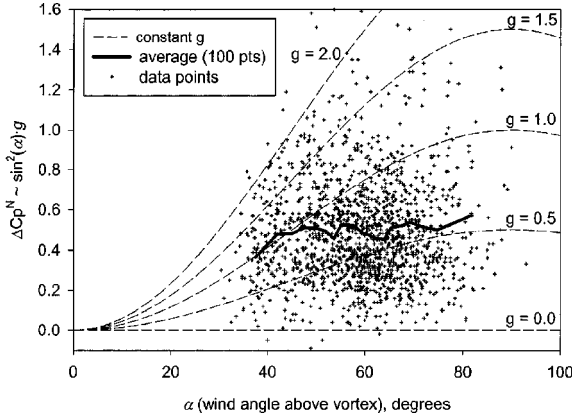
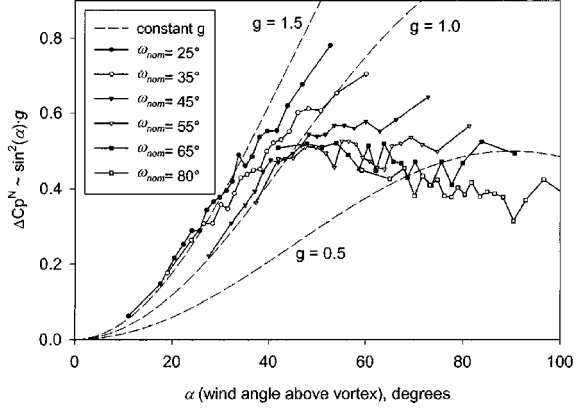
The calculation of  $g(t)$  from Eq. (3) requires a division by  $\sin^2(\alpha)$ , which for low  $\alpha(t)$  values can lead to large values of  $g(t)$ . As a result, it has been found to be more revealing to plot  $\Delta Cp^N(t)$  vs.  $\alpha(t)$ , where  $\Delta Cp^N(t)$  is given by

$$\Delta Cp^N(t) = (1 - Cp_s^N(t)) \cdot \left( \frac{\bar{U}_{ref}^2}{\bar{U}_M^2(\omega(t))} \right) - 1 \quad \text{with} \quad Cp_s^N(t) = Cp_s(t) \cdot \left( \frac{\bar{U}_M(\omega(t))}{U_M(t)} \right)^2 \quad (4)$$

and the superscript  $N$  indicates a Normalization by the local flow velocity.  $\Delta Cp^N(t)$  simply provides a means of experimentally estimating the value of  $\sin^2(\alpha) \cdot g$  from the  $Cp_s(t)$  and  $U_M(t)$  measurements.

The  $\Delta Cp^N(t)$  plots are compared with curves for  $\sin^2(\alpha) \cdot g$  for different constant values of  $g$  in Fig. 15, where tap #39 is the target tap. This plot is for a nominal wind direction ( $\omega_{nom}$ ) of  $55^\circ$ , where the value of  $\omega_{nom}$  is determined by the rotation of the wind tunnel's test section turntable. Recall that the value of  $g$  is expected vary between 0 (when there is no vortex present) and close to 1.5 (for a strong vortex). While there is considerable scatter in the data, most of the data points do stay within this range. This indicates that vortex strength, as indicated by the amplification factor  $g$ , varies on a continuum between 0 and a peak value, with a probability distribution that is essentially Gaussian. The fact that there are quite a few data points above the  $g = 1.5$  line suggests that this might be slightly low peak value estimate for a strong vortex. It is also worth noting that the scatter is in part attributable to the loss of correlation between  $U_M(t)$  and  $Cp_s(t)$  at higher frequencies, and that the values of  $g > 2$  are all but eliminated for most wind angles if the signals are filtered at 30 Hz.

For the plotted average in Fig. 15, the  $\Delta Cp^N(t)$  time series was sorted by  $\alpha(t)$  and then grouped; each point on the curve represents an average of 100 data points. Similar grouped-average curves were calculated for data from a range of  $\omega_{nom}$  data series, and the results are shown in Fig. 16. These curves illustrate the aforementioned inaccuracy of the quasi-steady theory. In a truly quasi-steady situation, all of the averaged  $\Delta Cp^N(\omega)$  points would fall on a common curve, regardless of  $\omega_{nom}$ . Instead, the curves run alongside each other, so that, for example, for  $\alpha(t) = 50^\circ$ ,  $\Delta Cp^N$  ranges from 0.75 for  $\omega_{nom} = 25^\circ$  to 0.5 for  $\omega_{nom} = 65^\circ$ . The general mean trend evident in each  $\omega_{nom}$  curve is, however, consistent with the quasi-steady expectation that as  $\alpha$  increases,  $g$  decreases. Looking at how  $\Delta Cp^N$  intercepts the  $g = \text{constant}$  lines for  $\omega_{nom} = 55^\circ$ , for example, we see  $g(t)$  decrease from 1.1 near  $\alpha(t) = 40^\circ$  to 0.6 at  $\alpha(t) = 75^\circ$ .


 Fig. 15  $\Delta C_p^N$  data for  $\omega_{nom} = 55^\circ$ . Target tap is tap #39

 Fig. 16 Group-averaged  $\Delta C_p^N$  curves for various nominal wind directions (tap #39)

The calculation of  $\Delta C_p^N$  ought to theoretically remove the influence of local velocity fluctuations on  $C_p(t)$ , allowing the influence of  $\alpha(t)$  and  $g(t)$  on  $C_p$  to become evident. This is true in a general sense: In Fig. 16, it is seen that for  $\alpha < 40^\circ$ , the fact that  $\sin^2(\alpha(t)) \rightarrow 0$  forces  $\Delta C_p^N$  towards 0, while it is the falling value of  $g(t)$  as  $\alpha \rightarrow 90^\circ$  that keeps  $\Delta C_p^N(t)$  below 0.5. However, the calculation of  $C_p^N(t)$  involves the division of  $C_p(t)$  by  $U_M^2(t)$ , and the resulting correlation coefficient between  $C_p^N(t)$  and  $U_M(t)$  is typically 0.30. As a result,  $g(t)$  still varies somewhat with  $U_M$ , and since  $U_M$  is a function of the wind direction, a spurious correlation is introduced between  $g$  and  $\alpha$ .

To ensure that higher  $g$  values were not simply the result of the residual influence of  $U_M$ , and so to better isolate the effect of  $g$  on  $C_p$ , selected data with  $0.9 < U_M / \bar{U}_M < 1.1$ , and  $\alpha$  in the range  $\bar{\alpha} \pm 8^\circ$  were used to calculate  $g$  for several nominal wind directions. The resulting  $g(t)$  values and their associated row #3  $C_p$  profiles (usually around 1000 data points) were sorted by  $g(t)$ , and consecutive groups of 50 were averaged to produce Fig. 17. The results show that not only are  $|C_p|$  values greater for higher values of  $g$  (as would be expected from Eq. 3), but that the  $C_p$  profile shape changes with  $g$ . As  $g$  becomes smaller, the profile becomes flatter, while for large  $g$  values, the transition from peak suction to low suction is very sudden.

The flow structures associated with these  $C_p$  profiles can be examined through the simultaneously recorded flow velocities, surface pressures and flow images. Some sample images are shown in Fig. 18, which have a similar format to Fig. 7. Two hot-wire probes are evident, one along the roof and the other above the leading edge at the point C, and flow velocity vectors for the latter probe have been superimposed. Image exposure times were 1/125th of a second for (a) and (b), and 1/250th of a second for (c) and (d). Mean flow velocity at the point C was 11.4 m/s, and is indicated by the grey circle around the top hot wire probe. The nominal wind angle is  $45^\circ$ , and the reference flow velocity is 8 m/s at roof height.

Instantaneous concurrent flow velocities at C normalize the  $C_p$  values for each time step, so that the plots represent.

$$C_{p_{tap}}^N = C_{p_{tap}}(t) \cdot \left( \frac{\bar{U}_C}{U_C(t)} \right)^2$$

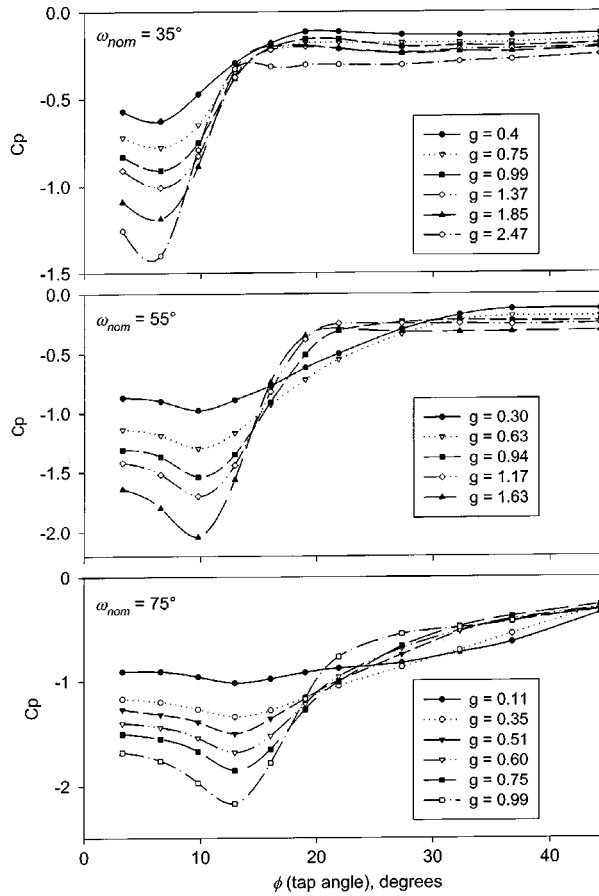


Fig. 17 Pressure profiles beneath row #3, sorted by the value of  $g$  (only includes data with  $|\alpha(t) - \text{mean}(\alpha)| < 8^\circ$  and  $.9 < U_M / \text{mean}(U_M) < 1.1$ )

The  $C_p^N = -1.0$  line is shown in grey, and is labeled “instantaneous  $C_p = -1.0$ ”. The rooftop corresponds to  $C_p^N = 0$ , and the bottom of the image corresponds to  $C_p^N = -2.1$ , as indicated. The square of the velocity ratio used to “correct”  $C_p(t)$  is indicated in the lower left corner, along with the image number and the mean flow velocity at  $C$  during the image. For row #5 and  $\omega = 45^\circ$ ,  $C_p^N = -1$  corresponds roughly to  $g = 0.4$ , and  $C_p^N = -2.1$  corresponds roughly to  $g = 1.9$ .

Images (b) and (d), with  $g > 1.5$ , clearly display vortices above the peak suction locations, while images (a) and (c), with  $g < 0.5$ , show little or no evidence of reattachment. In general, a high value of  $g$  and the associated rapid pressure recovery for  $\phi > \phi_C$  is seen in images with a distinct vortex and a clear reattachment point. Low  $g$  values are observed when there is either no vortex, or when there is a poorly defined vortex with a gradual pressure recovery and a reduced value of  $C_{pS}$ .

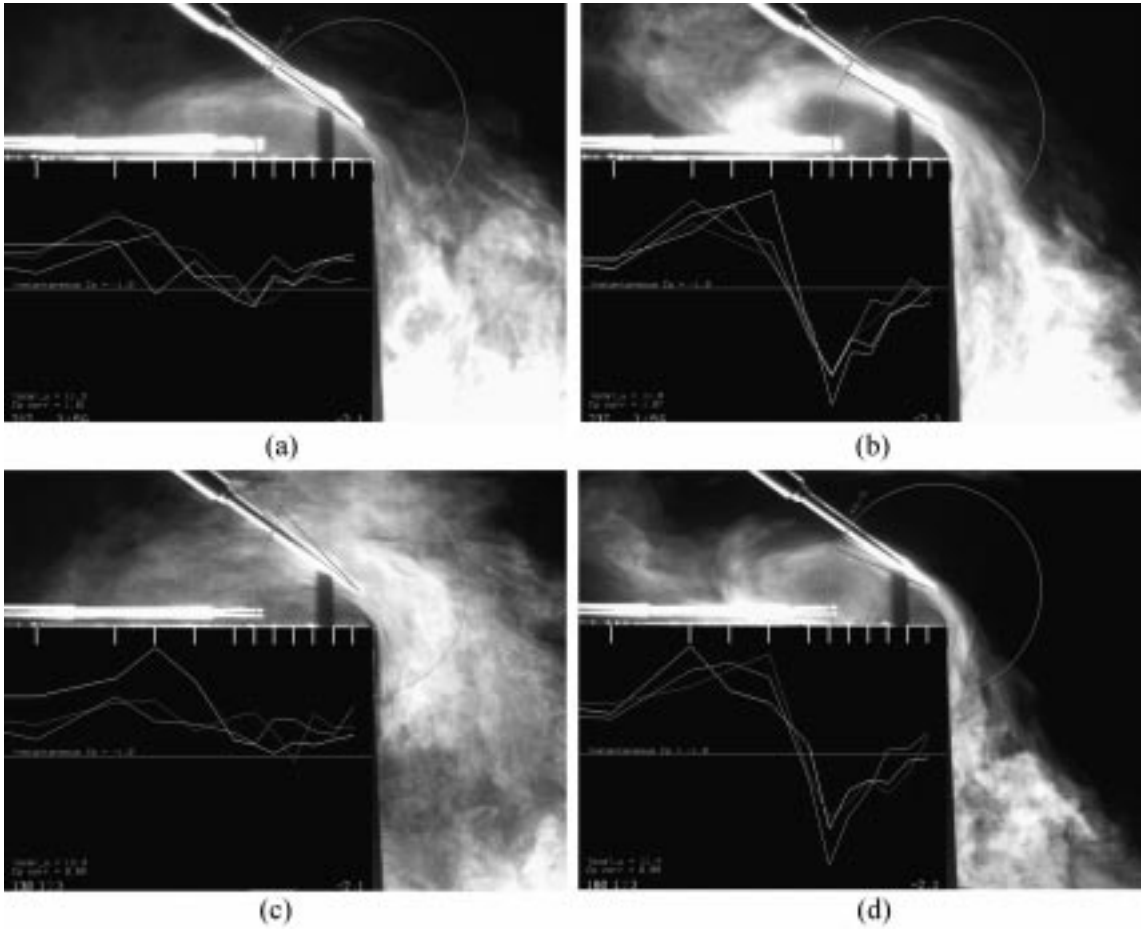


Fig. 18 Images of flow above the roof edge, using a light sheet along tap row #5, and showing simultaneously measured pressure profiles and flow velocities. The images illustrate the difference between low  $g$  (a and c) and high  $g$  (b and d) flows.

## 4. Discussion of some implications of the model

### 4.1. Frequency considerations

We surmise that the changes in the quality of the reattachment (and in the attendant value of  $g$ ) shown in Fig. 18 are linked in part to the presence of small-scale turbulence in the shear layer above the vortex. Melbourne (1993) and Gartshore (1973) have pointed out that for the separation bubble at the leading edge of a flat plate, the smaller separation zones (which are associated with higher surface suction) are instigated by small-scale turbulence, which increases the entrainment in the shear layer. We expect this to be true for the conical vortex as well. If the amount of small-scale turbulence at  $U_M$  were a function of time, then the vortex strength, dictated by the reattachment, would also vary rapidly in time. An examination of the simultaneous pressure profiles recorded during this study revealed that changes in vortex reattachment occur very quickly ( $fH/U > 3$  at  $x/H$

= 1.4). A normalized frequency of  $fH/U > 3$  at this location implies a length scale smaller than the circumference of the vortex.

Data reported by Li and Melbourne (1995) for bubble separation shows that for a constant level of turbulence intensity ( $I_u = 8\%$ ), increasing the integral scale ( $L_x$ ) had no effect on mean suction (or on the mean reattachment point) until  $L_x$  exceeded the re-attachment length, which is approximately equal to the vortex circumference. At this point, the mean suction decreased as the separation bubble became larger. This can be interpreted to imply that once  $L_x$  was sufficiently large, the level of this “small-scale” turbulence (of the size of the shear layer thickness) was reduced, and so the reattachment length increased.

Interestingly,  $Cp_{rms}$  stopped increasing with  $L_x$  at this point also. While this was not generally the case (for higher levels of  $I_u$ ,  $Cp_{rms}$  continued to increase as  $L_x$  became greater than the reattachment length), it highlights the difficulty of assessing the effects of turbulence on fluctuating pressures. This is perhaps because increasing one size of turbulence at the expense of another can have offsetting effects, since all gust sizes tend to increase  $Cp_{rms}$ :

- As noted above, small-scale gusts will determine the likelihood of a strong vortex. Without a strong vortex to amplify their effects, larger gusts will have less effect on surface pressure under the separated flow. The rapid changes in reattachment noted above will also result in vortex motion, which increases  $Cp_{rms}$ .
- “Medium-scale” gusts (of a size larger than the separation zone but smaller than the building) would be expected to increase the speed of the vortex rotation, without affecting the curvature. This is the classic quasi-steady  $I_u \cdot Cp$  contribution to  $Cp_{rms}$ . An increase in the frequency of this size of gust would also be expected to increase the relative size of the peak suction (Peak minimum  $Cp$  / mean  $Cp$ ), since each gust of this size is amplified by the curving separated flow. This was observed as  $L_x$  moved into this scale in the study by Li and Melbourne (1995).
- “Large-scale” gusts (of a greater size than the building) not only rotate the vortex faster, they also move the vortex. It is the motion of the high pressure-gradient reattachment zone across a tap which is sometimes the biggest factor in the value of  $Cp_{rms}$  (Banks and Meroney 2000a). (As a result, the location of peak  $Cp_{rms}$  on the roof is a good indicator of the mean location of reattachment.). This is the classic quasi-steady  $I_v \cdot dCp / d\theta$  contribution to  $Cp_{rms}$ .

As a result, the simulation of all scales of turbulence in the oncoming flow are important in reproducing suction beneath the conical vortex. Small-scale velocity fluctuations (especially the vertical component) are expected to influence entrainment, and so control the shape of the re-attachment zone. (It is worth considering that some portion of the turbulence at this scale could be generated by the leading edge itself). Medium-scale velocity fluctuations (especially the lateral component), are expected to accelerate the vortex spin, without changing its position or size. (This could explain why “fast and large” wind direction changes (short duration, large angle change), in which the wind briefly flows normal to the leading edge, have been observed to produce suction peaks (Zhao *et al.* 2000)). Large-scale lateral velocity fluctuations (i.e., wind direction shifts) will cause the vortex to move its position. In the case of shifts approaching  $\omega = 90^\circ$ , these gust can make the vortex unstable enough to disappear entirely, a phenomenon sometimes referred to as vortex “washout”. Longitudinal or stream-wise gusts of all scales larger than the vortex circumference will influence vortex rotation speed.

Note that the vortex circumference increases with distance from the apex. This suggests that as the apex is approached, it becomes increasingly important to simulate smaller and smaller scales of turbulence in order to reproduce peak pressures, as the definition of “small-scale” and “medium-

scale” scale with  $x$ .

#### 4.2. General considerations

- (1) Eq. (3) suggests that a quasi-steady type relationship exists between the local turbulence and the surface pressure under the vortex, with the longitudinal turbulence influencing  $C_p(t)$  through the  $U_{spin}(t)$  term and the lateral turbulence controlling  $C_p(t)$  via the  $\alpha(t)$ ,  $g(t)$  and  $U_M(\omega)$  terms. This possibility is considered in detail in another paper (Banks and Meroney 2000a).
- (2) The model does not explicitly contain any connection between vortex size and suction beneath the vortex. We speculated that if the roof surface boundary layer directly above the point S were to have a constant thickness regardless of vortex size, then more of the core suction might get passed on to the surface for smaller vortices, leading to higher  $g$  values at the surface. However, the data indicate that increased suction for smaller vortices near the apex can be essentially accounted for by the fact that  $U_M/U_{ref}$  is higher (recall Section 3.2).
- (3) If all of the core suction were passed on to the roof surface, the value of  $g$  would be 2.2, based on the inner vortex velocity profile given in the companion paper. This puts a limit on the lowest surface  $C_p$  considered possible for this model, using the profiles from the companion paper. If the turbulence intensity were 25%, for example, even if the entire core suction were passed on to the surface,  $C_p(t)$  would be  $-19$  right at the roof apex for a gust speed three standard deviations above the mean. However, if the  $U(a)$  velocity profile did not decrease as rapidly at  $a^{0.5}$ , higher core and surface suctions would be possible.
- (4) The vortices which form inside the separation bubble for flow normal to the roof edge ( $\omega = 90^\circ$ ) are also expected to be described by this model. Without the axial velocity to stabilize them, these vortices are more transient (so the mean value of  $g$  is lower), but the mechanism described by Eq. (3) should still apply. This explains the high peak  $C_p$  values measured for taps never under the conical vortex. They can experience the same momentary peak suction, since  $U_M/U_{ref}$  is still high (Fig. 11), and  $g(t)$  can still be 1.5 when a strong cylindrical vortex forms along the leading edge.
- (5) By tracking the position of the vortex core with a row of taps, it has been observed that while the peak  $C_p(t)$  values at a given tap are generally the result of a vortex being above that tap, the highest values of  $C_{p_{rms}}$  are largely related to the motion of the vortex. It is the repeated passage of the high pressure gradient reattachment over a tap which creates the largest  $C_{p_{rms}}$  values. The motion of the vortex is in part random, and is also controlled by the wind direction, or lateral turbulence. We speculate that the failure to match  $C_{p_{rms}}$  between full scale and model scale studies is therefore the result of the failure to adequately reproduce vortex motion.

#### 4.3. Practical considerations:

- (1) The extremely high  $y$ -direction pressure gradient associated with the strongest vortices could be a cause for concern from a design perspective. There the low reattachment suction may pressurize the bottom surface of a roofing paver, while the top surface experiences the full suction of the worst-case high- $g$   $C_{p_s}$ .
- (2) The link between the highest suction vortices and a firm and immediate re-attachment also suggests that inhibiting the flow reattachment can mitigate the worst vortex induced rooftop suctions. This has been observed (Banks 2000).

#### 4.4. Recommendations for future tests

Some recommendations for future research based on the above observations:

- This model provides a mechanism which connects the flow velocity at the point  $M$  to the surface pressure. It remains to be explained how flow distortion by the building alters the velocities at  $M$  with respect to the upstream flow.
- Using a simultaneously sampled row of taps normal to the leading edge to is essential to understanding what the pressure at any given tap is doing. Without some knowledge of where the vortex is, a drop in  $C_{prms}$ , for example, could be the result of a change in mean vortex position, or in the amount of vortex motion, both of which could be result of altered upstream flow conditions. Without some knowledge of the vortex behaviour, correlations between upstream flow conditions and rooftop surface pressures become very difficult to interpret.
- The use of wavelet transforms to assess changes in the high frequency turbulence content of  $U_M$  could reveal a good deal about whether instantaneous changes in high frequency turbulence in the shear layer are controlling the curvature of the flow above the vortex, and thus the surface pressure beneath it.
- With the changes in vortex reattachment in the visualization plane occurring at  $fH/U > 3$ , they are difficult to observe on a 1:50 scale model with a camera frame rate of  $f = 60$  Hz ( $fH/U = 0.6$ ). Using a camera shutter speed of 250 Hz ( $fH/U = 2.5$ ) helped to isolate the features of the rapidly changing vortex, but an exposure time 4 ms and a time between frames of 17 ms meant that 76% of the image information was lost. Future tests could be conducted on a larger model to slow down the phenomenon, especially near the apex, where the changes in reattachment can be expected to be even more rapid.
- Extremely low  $C_p$  values ( $< -20$ ) have been measured at a new tap near the apex on the TTU WERFL site. While the flow velocities measured in the wind tunnel indicate that the flow model predicts the concurrent wind-tunnel  $C_{ps}(t)$  values quite well, it cannot theoretically account for such low  $C_p$  values. It is suggested that  $U_M/U_{ref}$  be measured at full scale. Differences between  $U_M/U_{ref}$  at full scale and model scale could explain a lot of the discrepancies between roof corner  $C_p$  values measured in the tunnel and those observed at full scale.
- Some observations at CSU lead us to speculate that  $U_M/U_{ref}$  increases with roof height for low-rise buildings. ( $U_{ref}$  is measured upstream at roof height.). This would account for the increase in rooftop suction for taller buildings (Lin *et al.* 1995). Measurements could be performed to confirm this.

## 5. Conclusions

A curvature based model for the relationship between local flow speed and roof surface pressure has been developed and evaluated. Measurements indicate that the increase in flow speed directly above the vortex at the point  $M$  accounts for the known increase in suction towards the roof corner, as  $x \rightarrow 0$ .

The suction beneath the vortices is also known to reach a maximum near a wind angle of  $60^\circ$ . Three factors are shown to contribute to this peak :

- The flow speed at  $M$  reaches a maximum for a wind direction near  $65^\circ$ .
- The flow component normal to the vortex core at  $M$  increases as the wind becomes more normal to

the roof's edge ( $\omega \rightarrow 90^\circ$ ); this is expected to spin the vortex more quickly.

- The likelihood of a solid, stable vortex reattachment decreases as  $\omega \rightarrow 90^\circ$ .

The presence of a solid and clear-cut reattachment, as seen in Fig 18b, is shown to be associated with a larger than average pressure drop across the vortex (which translates into a high value of the parameter  $g$ ), and can be identified by a more sudden drop in suction between the vortex core and the reattachment point. The flow model predicts that high values of  $g$  are associated with greater curvature above the vortex, and this is confirmed by the flow visualization.

The companion paper estimated the value of  $g$  at 1.5 for such a solid reattachment with its concomitant distinct vortex, based upon some assumptions about the curvature and velocity profiles across the vortex core. While the curvature and velocity profiles could only be directly verified above the vortex core, indirect measurements of  $g$  indicate that  $g=0$  for no reattachment and  $g=1.5$  for a solid reattachments are good estimates.

The flow model suggests that all scales of turbulence play a role in determining the suction beneath the vortex, either by controlling the nature of the flow reattachment or by determining the speed at which the vortex spins. In the context of this model, further study of the connection between the components of turbulence at the point  $M$  and the upstream flow conditions should provide additional insight into the manner in which upstream flow conditions can control suction beneath rooftop conical vortices.

## Acknowledgements

The essential contributions of Dr. David E. Neff and Dr. Bernd Leitl in developing the experimental facilities at CSU are gratefully acknowledged. This work was supported by the US National Science Foundation grant number CMS-9411147 through the CSU-TTU Cooperative Program in Wind Engineering.

## References

- Banks, D. (2000), The Suction Induced by Conical Vortices on Low-Rise Buildings with Flat Roofs, Ph.D. dissertation, Civil Engineering Department, Colorado State University, Fort Collins, CO.
- Banks, D. and Meroney, R. N. (2000a), "The applicability of quasi-steady theory to pressure statistics beneath roof-top vortices", (accepted for publication) *Journal of Wind Engineering and Industrial Aerodynamics*.
- Banks, D. and Meroney, R. N. (2000b), "A model of roof-top surface pressures produced by conical vortices: model development", *Wind and Structures*, Accepted for publication,
- Banks, D., Meroney, R. N., Sarkar, P. P., Zhao, Z. and Wu, F. (2000), "Flow visualization of conical vortices on flat roofs with simultaneous surface pressure measurement", *J. Wind Eng. Ind. Aerodyn.*, **84**(1), 65-85.
- Gartshore, I. S. (1973) ,The effect of turbulence on the surface pressure field of a square prism, produced by University of Western Ontario, London, Ontario, BLWT-4-73.
- Ginger, J. D. and Letchford, C. W. (1992), "Peak wind loads under delta wing vortices on canopy roofs", *J. Wind Eng. Ind. Aerodyn.*, **41-44**, 1739-1750.
- Ham, H. J. (1998), Turbulence effects on wind-induced building pressure, Doctor of Philosophy, Civil Engineering, Colorado State University, Fort Collins, Colorado.
- Ham, H. J. and Bienkiewicz, B. (1998), "Wind tunnel simulation of TTU flow and building roof pressure", *J. Wind Eng. Ind. Aerodyn.*, **77 & 78**, 119-133.
- Letchford, C. W. and Marwood, R. (1997), "On the influence of v & w component turbulence on roof pressures beneath conical vortices", *J. Wind Eng. Ind. Aerodyn.*, **69-71**, 567-577.
- Li, Q. S., and Melbourne, W. H. (1995), "An experimental investigation of the effects of free-stream turbulence on streamwise surface pressures in separated and reattaching flows", *J. Wind eng. Ind Aerodyn.*, **54/55**, 313-323.

- Lin, J.-X., Surry, D. and Tieleman, H. W. (1995), "The distribution of pressure near roof corners of flat roof buildings", *J. Wind Eng. Ind. Aerodyn.*, **56**, 235-265.
- Marwood, R. and Wood, C. J. (1997), "Conical vortex movement and its effect on roof pressures", *J. Wind Eng. Ind. Aerodyn.*, **69-71**, 589-595.
- Melbourne, W. H. (1993), "Turbulence and the Leading Edge Phenomena", *J. Wind Eng. Ind. Aerodyn.*, **49**, 45-64.
- Minson and Wood (1992), "Investigation of separation bubbles and inclined edge vortices above model buildings using laser doppler anemometry", *11th Australasian fluid Mechanics Conference*, University of Tasmania, Australia.
- Saathoff, P. J. and Melbourne, W. H. (1989), "The generation of peak pressures in separated / reattaching flows", *J. Wind Eng. Ind. Aerodyn.*, **32**, 121-134.
- Zhao, Z., Sarkar, P. P. and Mehta, K. C. (2001), "Wind flow characteristics and their loading effects on low-rise building roofs", (submitted to) *Journal of Wind and Structures*.

## Notations

$a$	Normalized $z$ -direction distance from the core = $\zeta / h = (z - h) / h$
$C_1$	Arbitrary constant
$C_p$	Pressure coefficient = $(P - P_{ref}) / 0.5\rho(U_{ref})^2$
$C_{pM}$	$C_p$ at the point $M$ (directly above the vortex core)
$C_p^N$	$C_p$ corrected by the normalized local velocity
$C_{pS}$	$C_p$ at the point $S$ (on the roof surface, directly beneath the vortex core)
$f$	frequency
$g$	Integral of centripetal acceleration from inviscid region, through core, to roof
$g_s$	Value of $g$ at the point $S$
$h$	Height or distance of the vortex core above the roof surface
$H$	Building height
$I_u$	Longitudinal Turbulence Intensity = $\sigma_u / U$
$I_v$	Lateral Turbulence Intensity = $\sigma_v / U$
$k$	Arbitrary constant
$L_x$	Integral scale
$P$	Static pressure
$R_c$	Radius of curvature
$t$	Time
$U$	Flow speed
$U_{ref}$	Flow speed measured upstream at roof height
$U_{(point)}$	$U$ at the location (point) ex: $U_C, U_M$
$x$	Distance from the apex or leading corner, along the leading edge
$y$	Distance from the leading edge, along a line normal to the leading edge
$z$	Distance above the roof surface
$\alpha$	Wind angle above the vortex, relative to the vortex core axis
$\phi$	Angle with respect to roof edge; $\phi_c = \phi$ location of vortex core
$\Delta C_p^N$	Drop in $C_p^N$ from $M$ to $S$ due to vortex; see Equation (4)
$\theta$	wind direction relative to building or compass direction.
$\rho$	Air density
$\sigma_u$	Standard deviation of longitudinal flow speed
$\sigma_v$	Standard deviation of lateral flow speed
$\omega$	Wind angle relative to selected roof edge; $90^\circ$ is normal to the leading edge
$\omega_{nom}$	Nominal wind direction, determined by the orientation of the model building
$\zeta$	Distance from the vortex core, in the $z$ direction

Overbars indicate time averaged quantities.